Characterizing the Geometry and Quantifying the Impact of Nanoscopic Electrocatalyst/Semiconductor Interfaces Under Solar Water Splitting Conditions

John R. Hemmerling[1,2,3], *Aarti Mathur*[1,2,3], *Suljo Linic*[1,2,4]*

[1]Department of Chemical Engineering, University of Michigan, Ann Arbor, Michigan 48109, United States

[2]Catalysis Science and Technology Institute, University of Michigan, Ann Arbor, Michigan, 48109, USA

[3]These authors contributed equally to the work

[4]Lead Contact

*Correspondence: linic@umich.edu

Keywords: Photoelectrochemistry, interfacial physics, solar water splitting, nanoparticles

Abstract

Materials receiving the most attention in photoelectrochemical water splitting are metallic nanoparticle electrocatalysts (np-EC) attached to the surface of a semiconductor (SC) light absorbers. In these multicomponent systems, the interface between the semiconductor and electrocatalysts critically affect the performance. However, the np-EC/SC interface remains poorly understood as it is complex on atomic scales, dynamic under reaction conditions, and inaccessible to direct experimental probes. This contribution sheds light on how the electrocatalyst/semiconductor interface evolves under reaction conditions by investigating the behavior of nickel electrocatalysts (as nanoparticles and films) deposited on silicon semiconductors. Rigorous electrochemical experiments, interfacial atomistic characterization, and computational modeling are combined to demonstrate critical links between the atomistic features of the interface and the overall performance. It is shown that electrolyte-induced atomistic changes to the interface lead to (1) modulation of the charge carrier fluxes and a dramatic decrease in the electron/hole recombination rates and (2) a change in the barrier height of the interface. Furthermore, the critical roles of nonidealities and electrocatalyst coverage due to interfacial geometry are explored. Each of these factors must be considered to optimize the design

of metal/semiconductor interfaces which are broadly applicable to photoelectrocatalysis and photovoltaic research.

1. Introduction

Photoelectrochemical water splitting is one of the most promising chemical transformations to form renewable hydrogen. The key components of many water splitting photoelectrocatalysts are metallic electrocatalyst nanoparticles that are attached to the surface of a semiconductor light absorber.[1–3] In these multicomponent systems, the semiconductor absorbs photons, forming electron-hole pairs in which the electrons move to a hydrogen evolving electrocatalyst and holes move to an oxygen evolving electrocatalyst. The performance of nanoparticle electrocatalyst/semiconductor (np-EC/SC) photoelectrocatalysts is largely governed by the interface between the semiconductor and the

electrocatalyst as it governs the transfer of photo-excited electrons and holes from the semiconductor to the electrocatalyst and therefore the generated photovoltage which is one of the key performance metrics for solar water splitting performance.[4–9]

Despite the pivotal role of the np-EC/SC interface, its physical and chemical properties are poorly understood and difficult to characterize. The challenge is that the interface is complex on atomic scales and inaccessible to direct experimental probes. Furthermore, the interface may be dynamic under reaction conditions and the atomistic composition could be significantly different compared to as-prepared materials.[10,11] The atomistic changes to the interface can affect the work function, oxidation state, and catalytic function of the catalyst and semiconductor.[12–16]

In this contribution, we shed light on the complexities associated with the evolution of the np-EC/SC interface under photoelectrochemical water oxidation conditions. We do this by focusing on systems that contain planar Si semiconductor in contact with planar Ni electrocatalysts where the interface is effectively protected from the reactive electrolyte environment, and planar Si in contact with nanoparticle Ni electrocatalysts where the interface is exposed to the operating oxygen evolution reaction (OER) conditions. These Ni/Si photoanodes are of great interest for solar water splitting,[15,17–26] but the role of the interfacial layers is often neglected in the literature. To address this shortcoming, we observe that when exposed to electrolyte, there are significant atomistic changes to the interface manifested in the evolution of oxide phases. More importantly, we show that these atomistic interfacial features need to be built into any physical model that can capture the current-voltage behavior of these systems. For the first time for np-EC/SC systems, we show that the interfacial oxide layers play a critical role in (1) minimizing the electron/hole recombination by influencing the charge carrier fluxes and (2) modifying the barrier height of the EC/SC junction. The findings show that to capture and optimize the behavior EC/SC systems, the atomistic structure of the interface under reaction conditions needs to be characterized. These results offer new insights and design principles to optimize the charge carrier fluxes through EC/SC interfaces and therefore minimize recombination losses and maximize photovoltage in photoelectrocatalysts.

2. Physical, Electrochemical and Atomistic Characterization of Photoanodes

We fabricated and analyzed three experimental systems: (1) 5 nm of planar Ni film electrocatalyst evaporated on BHF-etched Si (pf-Ni/Si). Here, the native SiO_2 layer was removed from the Si surface by surface etching by BHF, (2) 5 nm of planar Ni film evaporated on Si with a native SiO_2 layer (pf-Ni/SiO_2/Si), and (3) nanoparticles of Ni electrodeposited on BHF-etched Si (np-Ni/Si). The data in **Figure 1a-c** show the OER performance under 1-sun illumination for each system. We measure the photovoltage by comparing the onset potentials (i.e., the voltage at 1 mA/cm^2) for illuminated n-Si samples and dark electrochemical p^+-Si control samples with identical Ni electrocatalysts for the respective samples. The data in Figure 1a show that pf-Ni/n-Si, exhibits poor performance, generating only ~65 mV photovoltage under solar illumination. On the other hand, pf-Ni/SiO_2/n-Si yielded a higher photovoltage of 230 mV. The data also show that np-Ni/n-Si generated an enhanced photovoltage of 480 mV, consistent with previous reports. [15,25] The redox peaks present prior to the onset potential in **Figure 1a-c** are attributed to the oxidation and reduction of the surface of the nickel electrocatalyst.

Figure 1d-e shows the scanning electron micrograph (SEM), top-down views of np-Ni/n-Si and np-Ni/p^+-Si systems (after the electrochemical cycling). For the electrodeposited Ni nanoparticles on both n-Si and p^+-Si, the average nanoparticle radius was 37.5±18.7 nm and 43.8±22.9 nm respectively and the nanoparticle size distributions are similar (Figure 1f), confirming that the p^+-Si samples are valid electrocatalytic controls for evaluating the photovoltage. The top-down SEM images also reveal that ~22% of the Si surface is covered by the Ni nanoparticles. Unlike the nanoparticle systems, the SEM images for the planar samples show minimal features indicating that the catalyst is planar and

covering 100% of the Si surface (see Supporting Information).

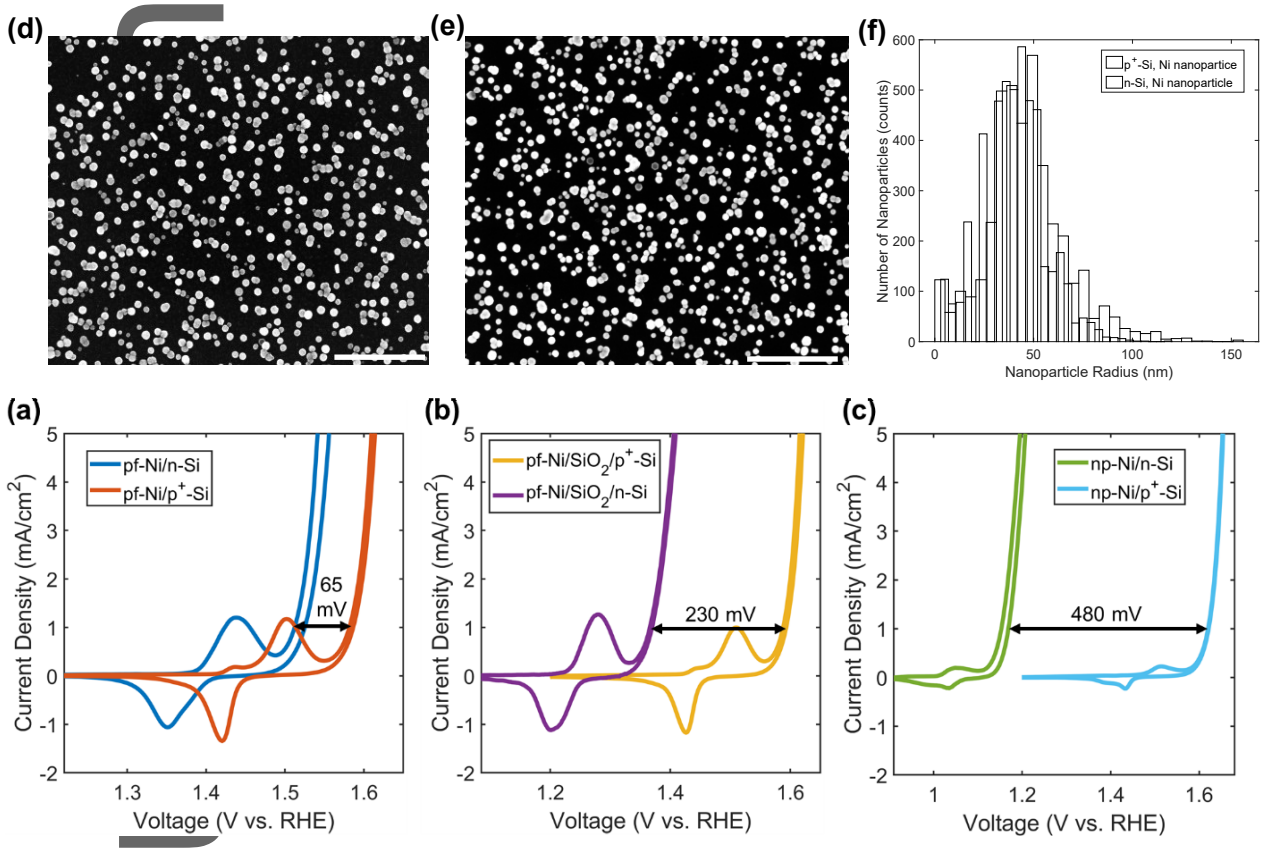

Figure 1: Water oxidation current density-voltage (J-V) plots measured at a scan rate of 50 mV/s of 1-sun illuminated photoelectrocatalysts and respective electrocatalyst control samples for (a) pf-Ni/Si, (b) pf-Ni/SiO_2/Si, and (c) np-Ni/Si collected after 30 voltage sweeps. The full voltage sweeps are

provided in the Supporting Information. (d) SEM characterization of a np-Ni/n-Si system after electrochemical testing. The data show an average particle radius of 35.7±18.7 nm and 20.7±0.3% coverage. Magnification is 25kx, and the white scale bar represents 2 micrometers. Comparisons between before and after electrochemical testing are provided in the Supporting Information. (e) SEM characterization of a np-Ni/p^+-Si system after electrochemical testing with an average particle radius of 43.8±22.9 nm with 22.9±1.8% catalyst coverage. Magnification is 25kx and the white scale bar represents 2 micrometers (f) Size distribution on Ni nanoparticle for np-Ni/Si systems.

We also monitored the performance of these systems over time after 3, 10, 20, and 30 potential sweeps. The data in Figure 2a show that under illumination the onset potential of each sample improves by ~3 mV for every ~10 voltage sweeps. The onset potential is governed by two factors: (1) the photovoltage generated by the system and (2) the electrocatalyst overpotential (i.e., the electrocatalytic performance of Ni). These contributions can be deconvoluted by comparing the n-Si and p^+-Si data in **Figure 2a, b.** For all p^+-Si systems, the electrocatalytic overpotential improves at the same rate as the onset potentials for the n-Si samples (~3 mV every 10 cycles). Meanwhile, the generated photovoltage for each system is largely unaffected by the voltage cycling (<1 mV every 10 cycles in Figure 2c). The onset potential improvement for each sample is therefore attributed to the increase in catalytic activity as more Ni is oxidized and incorporated with incidental Fe ions present in trace amounts from the electrolyte which has been previously demonstrated to improve the OER performance of Ni.[27] These trends also continue for longer term cycling and stability testing (see Supporting Information for details).

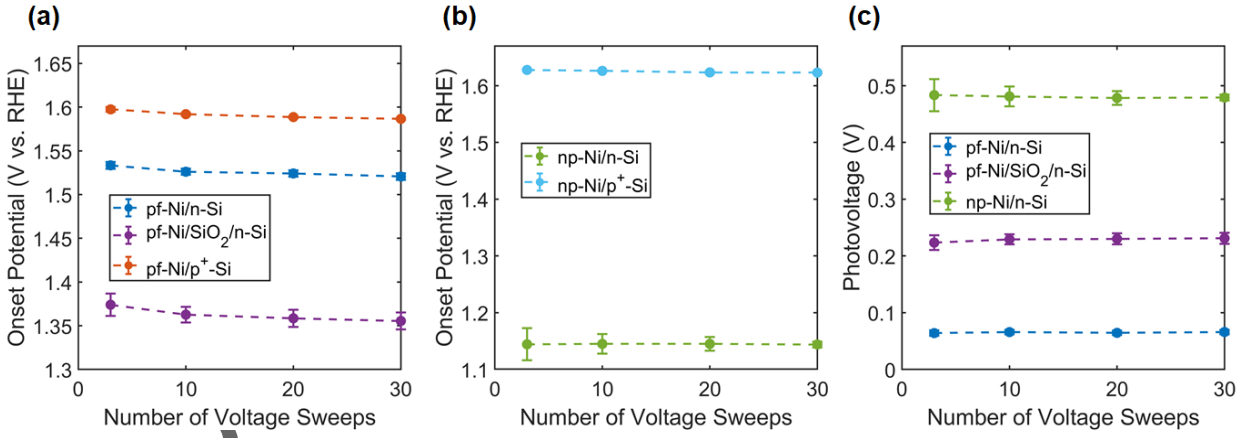

Figure 2: (a) Evolution of the onset potentials with respect to the reversible hydrogen electrode (RHE) after 3, 10, 20, and 30 voltage sweeps for 1-sun illuminated photoelectrocatalysts and respective dark electrocatalyst control samples for (a) pf-Ni/Si and pf-Ni/SiO_2/Si and (b) np-Ni/Si. (c) Photovoltage as a function of voltage sweeps for pf-Ni/Si, pf-Ni/SiO_2/Si, and np-Ni/Si systems, defined as the difference in onset potentials between the illuminated systems and respective dark electrocatalytic controls.

To understand the significant differences in the measured photovoltage for the three systems in Figure 1 and 2, we characterized the Ni/Si interface using scanning transmission electron microscopy (STEM) cross-sectional imaging. The STEM images of representative Ni nanoparticles on Si in **Figure 3a, b** show that the contact radius at the Ni nanoparticle/Si interface is significantly smaller than the nanoparticle radius. Specifically, the actual contact area of the Ni/Si interface is a factor of ~2 times smaller than the amount of Si surface that appears to be covered based on the SEM images in Figure 1d-f. Approximately 11% of the Si surface is in the direct contact with Ni (see Supporting Information for details).

We also performed elemental mapping of the interfaces for each photoelectrocatalyst system. Figure 3c, d show the cross-sectional STEM images for pf-Ni/Si and pf-Ni/ SiO_2/n-Si after electrochemical testing. In these planar systems, the Ni atoms at the surface of the Ni electrocatalyst that are directly exposed to the electrolyte are oxidized, but the electrolyte does not penetrate entirely through the Ni

film which leaves the underlying interfaces unaffected by the oxidizing electrolyte. STEM imaging of the pf-Ni/Si interface in Figure 3d shows a direct Ni/Si interface without detectable oxide layers. STEM imaging of the pf-Ni/ SiO_2/n-Si sample in Figure 3c, where Si contained a native SiO_2 layer before the Ni deposition, shows that the SiO_2 layer is 1.60±0.14 nm thick.

The STEM image in Figure 3e shows that as-deposited Ni nanoparticles on Si are in metallic state. On the other hand, Figure 3f shows that after OER testing, a thin NiO_x shell is formed, resulting in a core-shell Ni/NiO_x structure. This NiO_x shell is formed in-situ due to the interaction between the system and the electrolyte under the oxidizing conditions of OER. The thickness of the NiO_x shell surrounding the nanoparticles was measured to be ~2.4 nm. The cross-sectional images also show that the interface between the Ni and the Si is fully oxidized, i.e., there are NiO_x and SiO_2 layers that evolve. Comparing Figures 3e and 3f show that the as-prepared and used np-Ni/Si samples contained SiO_2 layers of similar thickness of 2.31±0.28 nm. This indicates that the SiO_2 layer is formed rapidly as BHF-etched Si is exposed to the electrolyte even during the electrodeposition of Ni nanoparticles. The data also shows that SiO_2 appears to be stable (i.e., not growing or being etched) throughout the timescale of the water oxidation experiments (30 voltage sweeps). We note that it is generally assumed in the literature that the interface does not change under the reactions conditions and in many cases a direct contact between pristine Si and metallic Ni is presumed in the analysis of these systems.[15,24–26] It is important to quantify how these atomistic features of the interface impacts the performance of the Ni/Si photoelectrocatalysts in OER. The interfacial changes that can play a significant role in affecting the photovoltage are:

(i) The formation of the interfacial NiO_x layers can lead to the change in the barrier height between EC and SC. For metal-EC/SC contacts, the equilibration between the SC and EC Fermi levels results in an electric potential barrier height that promotes the selective transfer of one charge carrier (in this case, holes) while impeding the transport of the opposite charge carrier.[28] This potential barrier (also known as the barrier height), governs the e^-/h^+ recombination rates and is dependent on the properties of the metal/semiconductor interface. A smaller barrier leads to higher recombination rates and photovoltage losses.

(ii) The formation of the interfacial SiO_2 layers can also impact the magnitude of the barrier height since the direct Si/Ni contacts can lead to formation of Ni silicide or the undesired Fermi level pinning.[29,30]

(iii) The formation of the thin SiO_2 insulator layers can lead to the change in the flux of energetic electrons and holes across the metal/semiconductor interface since these charge carriers need to tunnel through the insulator to reach the electrocatalyst. This also can affect the recombination rates and impact the photovoltage.[4,31–34]

(iv) The geometry of the interfacial contact area will also modulate the transfer of charge carriers across the interface, i.e., the rate of the collection of charge carriers by the EC is affected by the interfacial contact EC/SC area.[35]

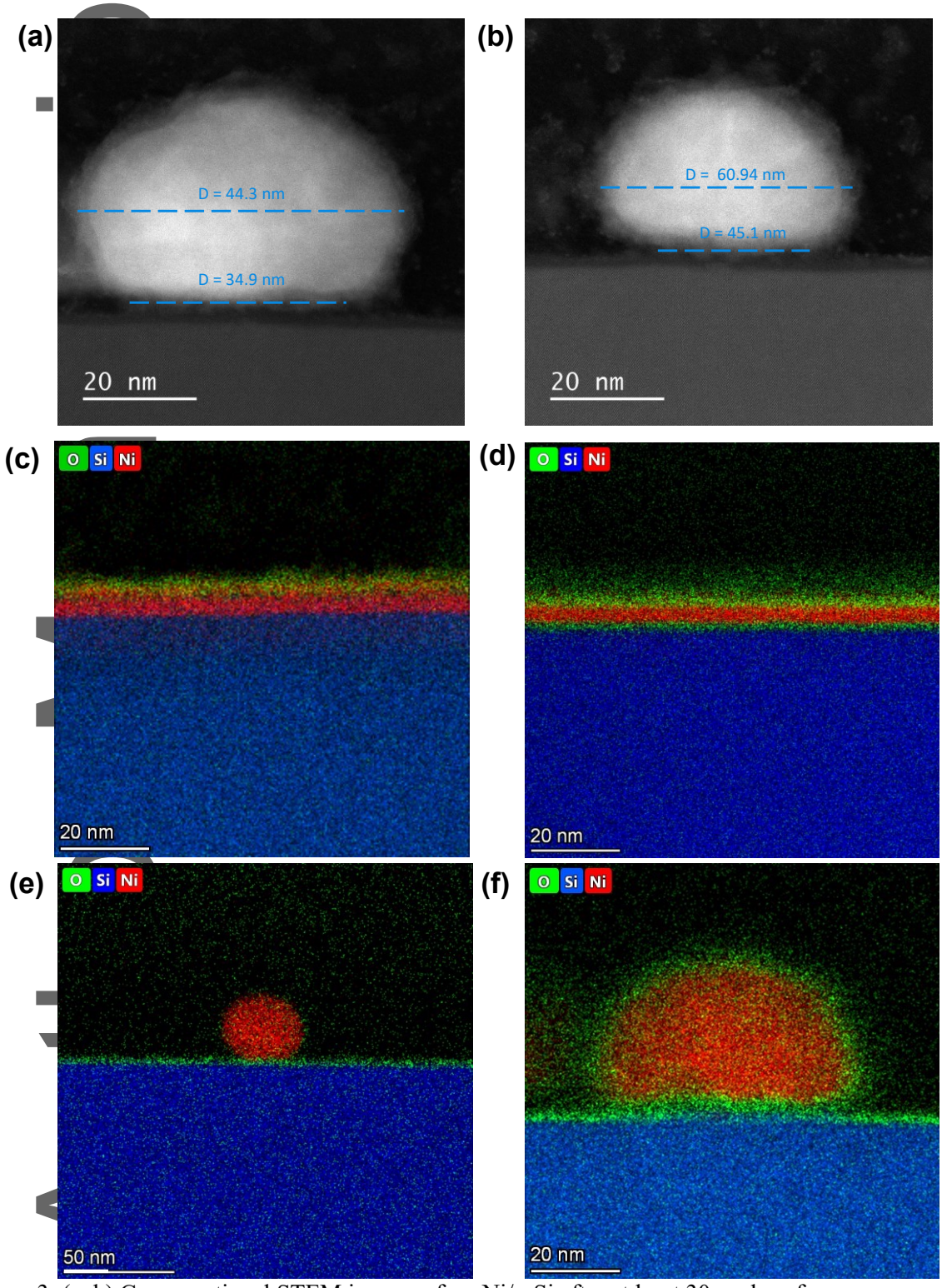

Figure 3: (a, b) Cross-sectional STEM images of np-Ni/n-Si after at least 30 cycles of

electrochemical testing demonstrates the difference in the actual contact radius compared to the nanoparticle radius. (c-f) Elemental mapping of the interface of: (c) tested pf-Ni/n-Si, (d) tested pf-Ni/SiO_2/n-Si, (e) as-deposited np-Ni/Si, (f) tested np-Ni/Si.

To test whether the barrier height is different for the oxidized Si interface in contact with Ni compared to the non-oxidized Si/Ni interface (mechanisms i and ii above), we performed the Mott-Schottky analysis (see Supporting Information for details). The measured Mott-Schottky barrier height of pf-Ni/Si was 0.59 eV which is consistent with previously reported values.[15,21] Such a low barrier height is typically attributed to Fermi level pinning or the formation of nickel silicide at the interface.[29,30] Meanwhile, the Mott-Schottky barrier height of the pf-Ni/SiO_2/n-Si was measured to be 0.67 eV. The SiO_2 interfacial layer modestly improves the Mott-Schottky barrier height, probably by preventing the formation of Ni silicide at the interface.[29,30] We note that the introduction of SiO_2 adversely impacts the ideality factor in the pf-Ni/SiO_2/n-Si system which negates the benefits of the increased Mott-Schottky barrier height (see Supporting Information and discussion below).[4,36]

While the heterogeneous nature of np-Ni/Si prevents us from directly evaluating the barrier height using Mott-Schottky analysis (i.e., a fraction of Si is covered by Ni and the rest with the electrolyte), it is reasonable to assume that the barrier height between Ni nanoparticles and Si is equivalent to the pf-Ni/SiO_2/n-Si barrier height since both contain SiO_2 interfacial layers which prevent Ni silicide formation. The np-Ni/Si systems, however, have an additional interfacial NiO_x layer that evolved under OER conditions, so we explored how NiO_x could impact the barrier height. We synthesized planar Si/SiO_2/NiO_x/Ni systems by oxidizing the Ni layers in the planar Si/SiO_2/Ni sample and depositing additional Ni layers on the NiO_x. The Mott-Schottky analysis showed that the barrier height was not enhanced by the interfacial NiO_x layer (see Supporting Information). This result suggests that the evolution of a thin NiO_x layer (~2.4 nm) in np-Ni/Si systems has a negligible impact on the barrier height of the much larger Ni nanoparticles (>30 nm radius). In other words the effective work function of the Ni nanoparticles is dominated by the thick Ni core rather than the thin interfacial NiO_x.[37] We also note the possibility that the pinch-off effect, induced by the evolution of a high work function NiO_x shell surrounding the Ni nanoparticles, may affect the photovoltage.[15] To investigate this possibility, we modeled these systems with COMSOL finite-element simulations, and the results demonstrate that the pinch-off effect is negligible for the nanoparticles dimensions studied herein (see Supporting Information for details). This was further supported by the experimental observation that

no photovoltage enhancement was seen as a function of voltage cycling (Figure 2c) despite the extensive oxidation of Ni over time, confirming that the evolution of NiO_x (which is not present in as-deposited samples) does not significantly impact the photovoltage. Therefore, we assume that in reacting environment the barrier height characteristics are similar for the np-Ni/n-Si and the pf-Ni/SiO_2/n-Si systems.

To summarize, the experimental data in Figures 1-3 show that: (1) due to the geometry of Ni electrocatalyst nanoparticles, the EC/SC contact area is significantly lower than the area outlined by the circumference of the nanoparticles. In our example of np-Ni/n-Si, while ~22% of the Si surface appears to be covered by Ni nanoparticles from a top-down SEM view, a smaller fraction of the Si surface (~11%) is in direct contact with the nanoparticle electrocatalysts and (2) in the case where the electrolyte can reach the interface, there is a degree of oxidation of the interfacial Ni and Si atoms. The presence of the interfacial SiO_2 increases the Mott-Schottky barrier height from 0.59 eV for a direct Si-Ni contact to 0.67 eV for systems with the interfacial SiO_2. Furthermore, the presence of the SiO_2 insulator at the interface will impact the flow of energetic charge carriers, which now need to tunnel from the semiconductor to the electrocatalyst through the insulator.[4,34]

3. Modeling of the Photoelectrocatalysts Behavior

To describe and quantify how these atomistic changes to the EC/SC interface impact the system performance, we developed an analytical model that can capture the behavior of the systems. The model is based on the illuminated diode equation, in which the relationship between the photovoltage (V_{ph}) and the net current (J_{net}) through an EC/SC interface is given by the following expression:[31]

$$|V_{ph}| = \frac{nkT}{q}\left[ln\left(\frac{J_{ph}-J_{net}}{J_s}+1\right)\right] \quad 1$$

Where n is the ideality factor, k is the Boltzmann constant, T is temperature, J_{ph} is the photo-limited current density, and J_s is the dark saturation current which is related to the rate at which electrons migrate to the metal electrocatalyst and recombine with holes. J_s is a critical parameter governing the

e^-/h^+ recombination rates and the generated photovoltage, and in general J_s needs to be minimized to maximize the system photovoltage. For the case of a planar metal/semiconductor interface (i.e., no interfacial insulator present), J_s can be evaluated using the following expression:[30]

$$J_s = A^* T^2 exp\left(-\frac{q\phi_b}{kT}\right) \quad (2)$$

Here, A^* is Richardson's constant, and ϕ_b is the equilibrium (zero-bias) barrier height which is defined as the difference between the Si conduction band and the effective work function of the Ni at the interface (see **Figure 4a**).

To capture the behavior of systems with Ni nanoparticles and the SiO_2 interfacial layer between Ni and Si, we need to account for a few physical changes compared to the planar systems with the direct Ni-Si contact. These changes include a different Ni/Si contact area (mechanism iv above) and a different barrier heigh. The interfacial SiO_2 insulator layer also limits the flow of charge carriers which must tunnel through the insulator to move from the semiconductor to the electrocatalyst (mechanism iii above).[4,38] To account for these changes, the equation describing the dark saturation recombination current needs to be modified to

$$J_s = f_c A^* T^2 exp\left(-\frac{q\phi_b}{kT}\right) \exp\left(-\propto d\sqrt{\phi_e}\right) \quad (3)$$

Here, f_c is the fraction of the semiconductor surface in direct contact with the catalyst ($f_c = 1$ for planar films, $f_c < 1$ for nanoparticles). These parameters are illustrated in Figure 4a. The second exponential term ($T_t = \exp\left(-\propto d\sqrt{\phi_e}\right)$) in eq. 3 is the probability that an electron will tunnel through the SiO_2 insulator and recombine in the metal, where $\propto$ is a constant, d is the insulator thickness, and ϕ_e is the offset between the insulator conduction band and semiconductor conduction band.[38] This probability is equal to 1 for the direct Ni-Si contact. For crystalline bulk SiO_2, ϕ_e exceeds 3 eV for an Si-SiO_2 contact, but the offset for non-crystalline, nanoscale SiO_2 is significantly lower.[39,40] Using previously described methodology,[31] we calculate the Si- SiO_2 insulator offset of 0.17 eV for the pf-Ni/SiO_2/Si system with measured SiO_2 thickness of 1.6 nm. These values yield a tunneling probability of 1.4×10^{-3}. Assuming the same 0.17 eV insulator offset for np-Ni/Si with a measured SiO_2 thickness

of 2.3 nm, the tunneling probability becomes 7.2×10^{-5}. These tunneling characteristics are comparable to previously reported probabilities obtained for ~2 nm thick SiO_2 on Si.[38,40,41]

By plugging equation 3 into equation 1, we can relate the photovoltage (V_{ph}) as a function of the net current density (J_{net}) density in which every parameter ($n, J_{ph}, f_c, \phi_b, d, \phi_e$) has been independently experimentally measured. To model J-V curves that can be compared to the experimental data, in addition to eq. 1-3, we introduce the contribution from the electrocatalytic reaction by fitting the dark p^+-Si control samples to the Butler-Volmer equation and using a series circuit approach as described previously[31] (see Supporting Information for details). Data in Figure 4b show the modeled J-V curves for the pf-Ni/SiO_2/n-Si system. The results show an excellent agreement between the experimental and modeled curves demonstrating that the model accurately reproduces the behavior of planar systems.

We have also modeled the J-V curves for the np-Ni/Si system using the same general procedure including the same barrier height and ideality factor as the pf-Ni/SiO_2/Si. The key differences are the measured EC/SC contact area (11% of the Si surface is in close contact with Ni) and the lower tunneling probability due to the thicker SiO_2 layer. Since there is a degree of uncertainty in the measured experimental parameters (particularly the SiO_2 thickness), we have also calculated the model's upper and lower bounds based on plus and minus one standard deviation (shaded region in Figure 4c). The data in Figure 4c show that the measured J-V curves are within the bounds of the model.

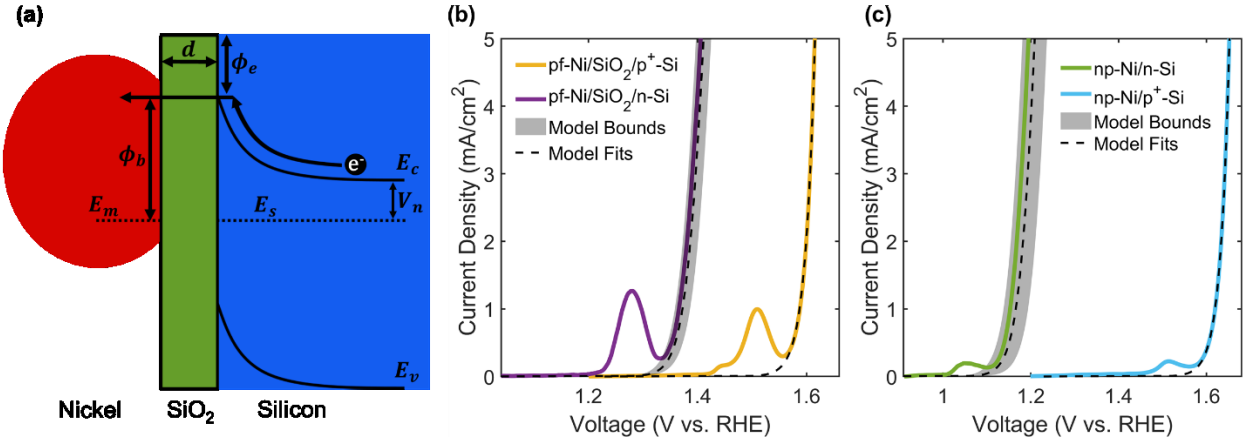

Figure 4: (a) Energy band diagram of a nanoparticle-based system that illustrates the key variable that affect the system performance. (b, c) Experimental current-voltage forward sweeps overlaid with the corresponding modeling results for (b) pf-Ni/SiO_2/Si and (c) np-Ni/Si. The shaded region represents the upper and lower bounds (plus and minus 1 standard deviation) of the modeling results based on the uncertainties of the experimentally measured parameters (see Supporting Information for details).

4. Analysis and Discussion

The modeling data shed light of how the interface geometry affects the performance of these systems. The analysis is captured in **Figure 5**. As we discussed above, the magnitude of the dark saturation current (J_s) governs the recombination rates and therefore losses in these systems. The saturation current for the baseline case of a planar metal/Si interface with a barrier height of 0 V equals A^*T^2 (1.1×10^{10} mA/cm^2). As shown in Figure 5, the existence of a potential barrier height decreases the recombination rates for all the systems by many orders of magnitude; however, a small barrier height cannot yield high photovoltages. This is the case for the pf-Ni/n-Si system where the direct Ni/Si contact has a low barrier height due to Ni silicide formation or Fermi level pinning. This low barrier height yields a low photovoltage of 62±4 mV.

The interfacial SiO_2 layer in the pf-Ni/SiO_2/n-Si systems affects the barrier height and the flux of charge carriers tunneling through the insulator. We measured that the SiO_2 layer slightly increases the Mott-Schottky barrier height, likely by preventing the formation of Ni silicide phases; however, we also measured that the presence of SiO_2 introduces nonidealities that offset these gains in the barrier height[4,31] (see Supporting Information for details). These nonidealities may manifest as a voltage drop within the SiO_2 insulator layer which lowers the barrier height and leads to the undesired recombination losses.[31,36,38] More importantly, we find that the most critical role of the SiO_2 layer is that it limits the dark saturation recombination current (through the tunneling probability term in equation 3) which dramatically improves the photovoltage. Specifically, the tunneling probability term (T_t) for the 1.6 nm thick SiO_2 layer (measured for pf-Ni/SiO_2/Si) decreases the recombination current (by lowering the undesired flux of energetic electrons from SC to EC) by a factor of ~700 (Figure 5), yielding a higher modeled photovoltage of 220±12 mV which matches the experimental photovoltage of 230±10 mV.

A significantly higher photovoltage totaling 480 mV was measured for np-Ni/n-Si. In these systems, the SiO_2 interfacial layer was approximately 2.3 nm thick (Figure 3e, f). Due to the exponentially lower tunneling probability through a 2.3 nm SiO_2 layer, the recombination current is predicted to decrease by a factor of 20 compared to the 1.6 nm SiO_2 layer. This thicker SiO_2 layer results in an additional ~130 mV photovoltage enhancement compared to the thinner SiO_2 layer that is present in pf-Ni/ SiO_2/n-Si.

Besides the tunneling probability, an additional decrease in the recombination current by a factor of ~9 is attributed to the fact that only ~11% of the Si surface is in close contact with the Ni. This leads to an increase in the photovoltage by ~110 mV compared to an identical planar system with 100% catalyst coverage. These combined characterization, modeling, and experimental efforts yield a predicted photovoltage of 456±28 mV, which agrees well with the experimental photovoltage of 480 mV.

It is important to analyze the above-presented results with respect to previous studies of EC/SC junctions. We show that the critical features governing the photocatalytic performance of these systems that are affected by the operating environment include the barrier height and the tunneling probability. While previous reports have speculated on the role of the interfacial layers,[24,42] the analysis presented above is the first to fully characterize these interfaces at atomistic levels and quantify their role in modulating the performance of the np-EC/SC system. Also, the prevailing view in the literature is that the high photocatalytic performance of np-EC/SC (e.g., np-Ni/n-Si) water oxidation systems compared to pf-Ni/n-Si can be attributed to the pinch-off effect which is described by the formation of a high work function NiO_x semi-shell surrounding the metallic Ni nanoparticles (i.e., a high barrier oxide shell surrounding a low barrier metal nanoparticle, with both interacting with Si at the interface).[15,17,18,20,24] Our data and analysis above show that the entire np-EC/SC interface is rapidly oxidized, and it is not necessary to invoke the pinch off effect when describing the performance of np-Ni/n-Si systems. The data can be well captured by quantifying the role of the oxidized interfacial layers that evolve in these systems as a water reactant reaches the interfacial sites. Our analysis presented above is further supported by COMSOL modeling (see Supporting Information) that shows that the pinch-off effect is relatively small even for the cases of rather small ~15 nm Ni particles surrounded by a ~10 nm NiO_x shell. We note that in the COMSOL analysis we used the highest possible band bending at the Si/NiO_x interface. In other words, the pinch-off effect as

traditionally described in the literature cannot explain the experimental photovoltage for our systems since the low barrier associated with the direct Ni/n-Si contact leads to elevated saturation currents. Overall, the data discussed above identifies a number of design approaches that can be used to enhance the photovoltage of EC/SC photoelectrocatalysts, including (1) decreasing the EC/SC contact area, (2) introducing an interfacial insulator layer with lower electron tunneling probability, (3) using alternative high work function metals that have an inherently higher barrier height (such as Ir), and (4) introducing a high-quality interfacial layer that minimizes defects (more ideal interface). By implementing these strategies, the photovoltage can exceed 600 mV, approaching the limit of the flat-band potential.[31]

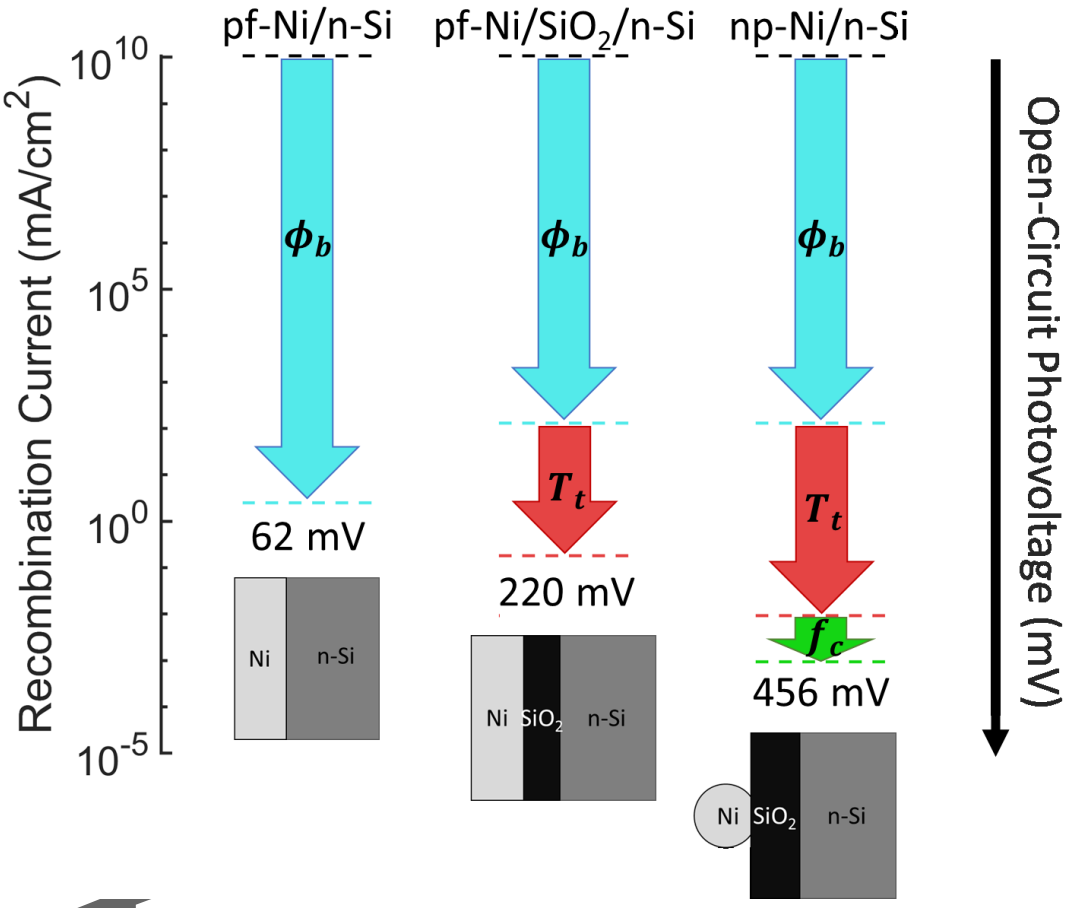

Figure 5: Modeled dark saturation recombination current densities evaluated at equilibrium and modeled photovoltages for each of the fabricated systems. The blue dashed lines represent the

recombination current considering only the barrier height. The red dashed lines represent the recombination current after additionally accounting for the impact of the SiO_2 layer which limits the probability that the electrons will tunnel through and recombine in the metal. The green dashed represents the recombination current after additionally accounting for the effect of catalyst coverage.

5. Conclusions

In this contribution, we experimentally compared the performance of planar nickel and nickel nanoparticle electrocatalysts deposited on Si photo-absorber to demonstrate the pivotal role of the interfacial layer in modulating the recombination rates for Ni nanoparticles on Si. We demonstrate that to rigorously capture and explain the behavior of EC/SC water splitting photoelectrocatalysts under reaction conditions it is necessary to unearth the atomistic features of the interface between nanoscopic electrocatalysts and semiconductor light absorbers. Our combined experimental and modeling efforts show that the combination of low catalyst/semiconductor contact area and the formation of the interfacial SiO_2 layer, which forms when the interface is exposed to water-based electrolyte, significantly improve the performance of Ni/Si photoelectrocatalysts. The main mechanism by which the interfacial SiO_2 affects the performance is that it suppresses the undesired electron flux from SC to EC. This electron flux would otherwise recombine with holes and decrease the photovoltage. We also show that under reaction conditions, a nickel oxide shell forms, completely surrounding the Ni metallic core. While the formation of the NiO_x phase that has a small positive impact on the catalytical activity, it does not significantly impact the barrier height and the generated photovoltage. Each of the factors discussed herein, particularly the role of interfacial insulator layers, must be quantified to understand, and accurately predict their performance of photoelectrocatalysts. Overall, the insights from this work based on in-depth modeling and rigorous experimental validation can be used to guide the design of a variety of photoelectrocatalysts as well as photovoltaics in which interfacial structures play a pivotal role.

6. Experimental Section/Methods

Resource Availability:

Lead Contact

Further information and requests for resources should be directed to and will be fulfilled by the Lead Contact, Suljo Linic (linic@umich.edu).

Materials Availability

This study did not generate new unique reagents.

Data and Code Availability

The data that support the findings of this study are available from the corresponding author upon reasonable request.

Nickel Nanoparticle and Planar Sample Fabrication

Phosphorous doped (n-type, resistivity 0.1-1 ohm-cm, (100)-oriented, 525 um thick) and boron doped (p-type, resistivity 0.001–0.005 ohm-cm, (100)-oriented, 525 μm thick) Si wafers were purchased from Addison Engineering. The Si wafers were hand-diced to 12x12 mm square pieces for all samples.

For pf-Ni/Si systems, Si pieces were cleaned with NanoStrip (a commercial piranha solution) for 10 minutes at room temperature and etched in buffered hydrofluoric acid (BHF) for 2 minutes to remove the native silicon oxide layer. For pf-Ni/SiO2/Si, Si pieces were sonicated in isopropanol for 10 minutes and rinsed with water (18.2 MΩ-cm). These were not etched to preserve the native SiO_2 layer. Ni planar films were deposited simultaneously in the same chamber for pf-Ni/Si and pf-Ni/SiO2/Si samples. Ni was e-beam evaporated (base pressure 2.5e-6 Torr) on Si pieces at a rate of 1 Å/s to a target thickness of 50 Å which was monitored by a quartz crystal microbalance.

Fabrication procedures for np-Ni/Si was adapted from previous works. Si pieces were cleaned using piranha solution (3/1 by volume concentrated aqueous H_2SO_4/30% aqueous H_2O_2) for 15 minutes and etched in buffered hydrofluoric acid for two minutes. Nickel was electrodeposited on wafer pieces using a solution of 0.01M $NiCl_2$ and 0.1M boric acid (H_3BO_3). Nickel chloride and boric acid were purchased from Sigma Aldrich with 99.95% and 99.5% purity respectively. The solution was sonicated for 10 minutes and then stirred for 5 minutes before electrodeposition. An Ag/AgCl reference electrode (Pine, FODR-0021) and platinum wire were placed in the electrodeposition solution. The position of the reference electrodes was kept constant from sample to sample. The wafer

piece was scratched using a diamond tip scribe, excess silicon dust was removed, and gallium-indium eutectic paint (99.99%) was applied to the scratched area to ensure an ohmic contact. The prepared wafer piece was then housed in a 3-D printed electrode with an O-ring and aperture of 0.459 cm^2 exposed to the electrolyte. The back contact was placed against a copper plate.

Once the electrode was submerged in the electrodeposition solution, EIS was used on each sample to evaluate the overall resistance, which includes the solution resistance and the resistivity from the wafers. The applied voltage selected for the electrodeposition was then selected b accounting for the ohmic losses such that the chronoamperometry plot is consistent from sample to sample and between the two semiconductor types. By accounting for the different resistance loses, the chronoamperometry plots for the n-Si and p^+-Si very closely overlap which results in comparable particle sizes and distributions. The applied voltage was adjusted for a final value of ~-1.5V vs Ag/AgCl for 5 seconds using a Gamry potentiostat. The sample was then rinsed with DI water and immediately tested electrochemically.

Electrochemical Testing

For all electrochemical experiments, samples were scratched, painted, and housed in a 3D printed electrode using the same method as nickel electrodeposited samples described above. The illuminated area and the area exposed to the electrolyte was defined by an O-ring with an area of 0.459 cm^2, and the current is normalized to this planar geometric area. All electrochemical experiments were performed using a three-electrode setup in a square quartz beaker.

For OER experiments, a 1M KOH electrolyte prepared using 45 wt.% KOH (Sigma Aldrich) and magnetically stirred. Samples were illuminated using a 300W UV 16S-Series Solar Simulator (Solar Light Company) with AM 1.5G filter. Light intensity was calibrated to 100 mW/cm2, or one sun, using a thermopile detector. N-type samples were illuminated during water oxidation measurements while p-type samples were measured in the dark. A graphite rod counter electrode and Hg/HgO (Pine, RREF0038) reference electrode were used to complete the three-electrode setup. Cyclic voltammetry was conducted at scan rates between 50-200 mV s^{-1}. Data in Figures 1 and 2 were obtained using 50 mV s^{-1}. For n-Si samples, voltages were typically cycled from -0.2V up to about 0.9V while for p^+-Si, voltages were typically cycled from 0V up to about 0.7V (Voltages are vs Hg/HgO). Voltages were

converted to RHE by calibrating the Hg/HgO reference electrode and accounting for the pH of 14 for the KOH.

$V_{vs.RHE} = V_{vs.Hg/HgO}$ + calibrated reference potential + 0.591*pH

For a typical set of OER experiments, the voltage was swept a total of 30 times. Then a few additional voltage sweeps as well as EIS measurements were performed to evaluate the solution resistance. All J-V cyclic voltammograms plots present are IR-corrected using the solution resistance. These tested samples were then rinsed with water and prepared for SEM and STEM analysis.

Mott-Schottky, EIS, and open-circuit voltage measurements for planar systems were conducted in a ferri-/ferrocyanide (FFC) solution consisting of 350×10^{-3} M potassium hexacyanoferrate(II) trihydrate, 50×10^{-3} M potassium hexacyanoferrate(III) (EMD Millipore), and 1 M KCl (Fischer Scientific). A graphite rod reference electrode and a Pt wire counter electrode were used to complete the three-electrode setup. The light intensity was varied using neutral density filters (Newport) which uniformly attenuate the incident light source over a broad range of wavelengths. In typical experiments, the light intensity is modulated between 0.6 Suns (60 mW/cm^2) and 1.5 Suns (150 mW/cm^2). At each light intensity, linear sweep voltammetry was performed with a scan rate of 100 mV s^{-1} to evaluate the photo-limited current density. The open-circuit photovoltage was measured before and after each linear sweep for about 60 seconds until stable values were reached. After varying the light intensity, the light was turned off and EIS measurements were performed at 0.1 V intervals between 0.2-0.8 V vs. Fe(CN)3-/4- with a frequency range of 1000 Hz to 100,000 Hz and an AC voltage of 10 rms mV. Each EIS measurement was fit to an equivalent circuit to determine the space charge capacitance needed for the Mott-Schottky plots (see Supporting Information for details).

Sample Characterization

Scanning electron microscopy were performed using the TSF Nova 200 Nanolab with an accelerating voltage of 5kV. Nanoparticle size, size distribution, and coverage were analyzed using IMAGEJ software. Scanning transmission electron microscopy (STEM) was performed with the TFS Talos F200X G2 to gather energy dispersive x-ray spectroscopy (EDS) and performed with a JEOL 2011 probe-corrected analytical electron microscope to gather high resolution interfacial images. STEM samples were prepared using focused ion-beam milling (FIB) on the TFS Nova 200 Nanolab. Samples

were tested under OER conditions for 30 voltage sweeps and subsequent EIS testing prior to STEM preparation. Oxide thicknesses were measured using STEM imaging high-resolution TEM imaging where the $Ni/NiO_x/SiO_2/Si$ interfaces are marked by changes in contrast and atomic lattice structure. The thicknesses were determined by analyzing several nanoparticle samples with IMAGEJ software. Additional detail on STEM image processing is provided in the Supporting Information.

Acknowledgements

This research was supported by the U.S. Department of Energy, Office of Science, Office of Basic Energy Sciences, under Award DE-SC0021362 (nanoparticulate work) and National Science Foundation (NSF, CBET-1803991) (planar system work). The authors acknowledge the Michigan Center for Materials Characterization for subsidizing us in the use of geometry characterization instruments through NSF grants #DMR-0320740 and #DMR-0723032.

Author Contributions

J.H and A.M. contributed equally to the work. J.H. fabricated, tested, and analyzed planar Ni based samples as well as developed the models for all systems. A.M. fabricated, tested, and analyzed nanoparticle Ni based samples as well as performed EDS analysis on all systems, conducted experiments and analyzed data. S.L. conceived the ideas and story behind the manuscript and supervised the project. All authors discussed the results and co-wrote the paper.

Declaration of Interests

The authors declare no competing interests.

References

[1] S. Zhong, Y. Xi, Q. Chen, J. Chen, S. Bai, *Nanoscale* **2020**, *12*, 5764.

[2] S. A. Lee, S. Choi, C. Kim, J. W. Yang, S. Y. Kim, H. W. Jang, *ACS Materials Lett.* **2020**, *2*, 107.

[3] Z. Wang, C. Li, K. Domen, *Chemical Society Reviews* **2019**, *48*, 2109.

[4] J. R. Hemmerling, A. Mathur, S. Linic, *Acc. Chem. Res.* **2021**, *54*, 1992.

[5] S. Cao, Z. Zhang, Q. Liao, Z. Kang, Y. Zhang, *Energy Technology* **2021**, *9*, 2000819.

[6] S. M. Thalluri, L. Bai, C. Lv, Z. Huang, X. Hu, L. Liu, *Advanced Science* **2020**, *7*, 1902102.

[7] Y. Kuang, T. Yamada, K. Domen, *Joule* **2017**, *1*, 290.

[8] Y. Chen, X. Feng, X. Guo, W. Zheng, *Current Opinion in Green and Sustainable Chemistry* **2019**, *17*, 21.

[9] J. Zhang, J. Cui, S. Eslava, *Advanced Energy Materials* **2021**, *11*, 2003111.

[10] C.-W. Tung, T.-R. Kuo, C.-S. Hsu, Y. Chuang, H.-C. Chen, C.-K. Chang, C.-Y. Chien, Y.-J. Lu, T.-S. Chan, J.-F. Lee, J.-Y. Li, H. M. Chen, *Advanced Energy Materials* **2019**, *9*, 1901308.

[11] F. Lin, S. W. Boettcher, *Nature Materials* **2014**, *13*, 81.

[12] S. Chen, L.-W. Wang, *Chem. Mater.* **2012**, *24*, 3659.

[13] M. T. Greiner, M. G. Helander, Z.-B. Wang, W.-M. Tang, Z.-H. Lu, *J. Phys. Chem. C* **2010**, *114*, 19777.

[14] A. Sivanantham, P. Ganesan, A. Vinu, S. Shanmugam, *ACS Catal.* **2020**, *10*, 463.

[15] F. A. L. Laskowski, S. Z. Oener, M. R. Nellist, A. M. Gordon, D. C. Bain, J. L. Fehrs, S. W. Boettcher, *Nat. Mater.* **2019**, 1.

[16] P. Nunez, M. Cabán-Acevedo, W. Yu, M. H. Richter, K. Kennedy, A. M. Villarino, B. S. Brunschwig, N. S. Lewis, *J. Phys. Chem. C* **2021**, *125*, 17660.

[17] K. Oh, C. Mériadec, B. Lassalle-Kaiser, V. Dorcet, B. Fabre, S. Ababou-Girard, L. Joanny, F. Gouttefangeas, G. Loget, *Energy & Environmental Science* **2018**, *11*, 2590.

[18] S. A. Lee, T. H. Lee, C. Kim, M. G. Lee, M.-J. Choi, H. Park, S. Choi, J. Oh, H. W. Jang, *ACS Catal.* **2018**, *8*, 7261.

[19] M. J. Kenney, M. Gong, Y. Li, J. Z. Wu, J. Feng, M. Lanza, H. Dai, *Science* **2013**, *342*, 836.

[20] F. A. L. Laskowski, M. R. Nellist, R. Venkatkarthick, S. W. Boettcher, *Energy & Environmental Science* **2017**, *10*, 570.

[21] S. Li, G. She, C. Chen, S. Zhang, L. Mu, X. Guo, W. Shi, *ACS Appl. Mater. Interfaces* **2018**, *10*, 8594.

[22] D. Liu, T. Jiang, D. Liu, W. Zhang, H. Qin, S. Yan, Z. Zou, *ChemSusChem* **2020**, *13*, 6037.

[23] Q. Cai, W. Hong, C. Jian, W. Liu, *Nanoscale* **2020**, *12*, 7550.

[24] G. Xu, Z. Xu, Z. Shi, L. Pei, S. Yan, Z. Gu, Z. Zou, *ChemSusChem* **2017**, *10*, 2897.

[25] G. Loget, B. Fabre, S. Fryars, C. Mériadec, S. Ababou-Girard, *ACS Energy Lett.* **2017**, *2*, 569.

[26] S. A. Lee, I. J. Park, J. W. Yang, J. Park, T. H. Lee, C. Kim, J. Moon, J. Y. Kim, H. W. Jang, *Cell Reports Physical Science* **2020**, *1*, 100219.

[27] S. Anantharaj, S. Kundu, S. Noda, *Nano Energy* **2021**, *80*, 105514.

[28] Z. Zhang, J. T. Yates, *Chem. Rev.* **2012**, *112*, 5520.

[29] R. T. (董梓則) Tung, *Applied Physics Reviews* **2014**, *1*, 011304.

[30] E. H. Rhoderick, *IEE Proceedings I - Solid-State and Electron Devices* **1982**, *129*, 1.

[31] J. Hemmerling, J. Quinn, S. Linic, *Advanced Energy Materials* **2020**, *10*, 1903354.

[32] J. Quinn, J. Hemmerling, S. Linic, *ACS Catal.* **2018**, *8*, 8545.

[33] J. Quinn, J. Hemmerling, S. Linic, *ACS Energy Lett.* **2019**, *4*, 2632.

[34] I. A. Digdaya, B. J. Trześniewski, G. W. P. Adhyaksa, E. C. Garnett, W. A. Smith, *J. Phys. Chem. C* **2018**, *122*, 5462.

[35] R. C. Rossi, N. S. Lewis, *J. Phys. Chem. B* **2001**, *105*, 12303.

[36] L. F. Wagner, R. W. Young, A. Sugerman, *IEEE Electron Device Letters* **1983**, *4*, 320.

[37] C.-H. Lu, G. M. T. Wong, R. Birringer, R. Dauskardt, M. D. Deal, B. M. Clemens, Y. Nishi, *Journal of Applied Physics* **2010**, *107*, 063710.

[38] H. C. Card, E. H. Rhoderick, *J. Phys. D: Appl. Phys.* **1971**, *4*, 1589.

[39] J. Robertson, *Journal of Vacuum Science & Technology B: Microelectronics and Nanometer Structures Processing, Measurement, and Phenomena* **2000**, *18*, 1785.

[40] L. C. Olsen, *Solid-State Electronics* **1977**, *20*, 741.

[41] H. C. Card, *Solid State Communications* **1974**, *14*, 1011.

[42] J. C. Hill, A. T. Landers, J. A. Switzer, *Nature Materials* **2015**, *14*, 1150.

Table of Contents Text:

We use electrochemical testing, atomic interfacial characterization, and computation modeling to elucidate the role of electrocatalyst/semiconductor interfaces under photoelectrochemical water oxidation conditions. We unearth the mechanisms by which the interface impacts the photovoltage and quantify the critical design parameters that must be optimized to improve performance. We also shed light on the impact of operating conditions on the interface.